# Quantum transport properties of $\beta$-$Bi_4I_4$ near and well beyond the extreme quantum limit

Peipei Wang,[1,2] Fangdong Tang,[2] Peng Wang,[2] Haipeng Zhu,[3] Chang-Woo Cho,[2] Junfeng Wang,[3] Xu Du,[4] Yonghong Shao,[1,*] and Liyuan Zhang[2,†]

[1]*Key Laboratory of Optoelectronic Devices and Systems of Ministry of Education and Guangdong Province, College of Optoelectric Engineering, Shenzhen University, Shenzhen 518060, China*

[2]*Department of Physics, Southern University of Science and Technology, Shenzhen 518055, China*

[3]*Wuhan National High Magnetic Field Center and School of Physics, Huazhong University of Science and Technology, Wuhan 430074, China*

[4]*Department of Physics and Astronomy, Stony Brook University, Stony Brook, New York 11794, USA*

(Received 5 February 2021; accepted 31 March 2021; published 8 April 2021)

We have investigated the magnetotransport properties of $\beta$-$Bi_4I_4$ bulk crystal, which was recently theoretically proposed and experimentally demonstrated to be a topological insulator. At low temperature $T$ and magnetic field $\boldsymbol{B}$, a series of Shubnikov–De Haas (SdH) oscillations is observed on the magnetoresistivity (MR). Detailed analysis reveals a light cyclotron mass of $0.1\,m_e$, and the field angle dependence of MR reveals that the SdH oscillations originate from a convex Fermi surface. In the extreme quantum limit (EQL) region, there is a metal-insulator transition occurring soon after the EQL. We perform scaling analysis, and all the isotherms fall onto a universal scaling with a fitted critical exponent $\zeta \approx 6.5$. The enormous value of critical exponent $\zeta$ implies this insulating quantum phase originated from strong electron-electron interactions in high fields. However, in the far end of EQL, both the longitudinal and Hall resistivity increase exponentially with $\boldsymbol{B}$, and the temperature dependence of the MR reveals an energy gap induced by the high magnetic field, signifying a magnetic freeze-out effect. Our findings indicate that bulk $\beta$-$Bi_4I_4$ is an excellent candidate for a three-dimensional topological system for exploring EQL physics and relevant exotic quantum phases.

DOI: 10.1103/PhysRevB.103.155201

## I. INTRODUCTION

Topological insulators (TIs) are quantum materials that have insulating bulk states and metallic surface states consisting of massless Dirac fermions [1–6]. The surface states are robust against time-reversal invariant perturbations and could lead to many interesting transport phenomena such as weak antilocalization [7–9,1–3], quantum oscillations [10–12], and the Aharonov-Bohm effect [13–15]. By far, bismuth-based binary or ternary compounds such as three-dimensional (3D) $Bi_{1-x}Sb_x$, quasi-2D $Bi_2Se_3$, $Bi_2Te_3$, and $Bi_2Te_2Se$ have become the essential class of TIs. These TIs have been studied extensively in past years and continue to attract research interest, due to promising both rich novel physics and potential applications in spintronics and quantum computation.

Recently, a new topological insulator $\beta$-$Bi_4I_4$ was theoretically predicted and experimentally confirmed [16–18]. However, angle-resolved photoemission spectroscopy (ARPES) experiments give different results about the topological classification of $\beta$-$Bi_4I_4$. Autès *et al.* performed the measurements on the (001) surface and revealed a single Dirac cone located at the $M$ point of the surface Brillouin zone [17], confirming $\beta$-$Bi_4I_4$ as a strong TI. But in a recent work, Noguchi *et al.* reported that only the side surface [the (100) plane] hosts the Dirac surface state, indicate that $\beta$-$Bi_4I_4$ is a weak TI [18]. Despite the ambiguity in its classification, $\beta$-$Bi_4I_4$ has shown many fascinating transport properties. Hysteretic profile forms at around 300 K on the resistivity-temperature curve, indicating a structural phase transition between $\beta$-$Bi_4I_4$ and $\alpha$-$Bi_4I_4$ [18]. The theoretical calculations and the experiments found a pressure-induced superconducting phase and multistructural or topological phase transitions in $\beta$-$Bi_4I_4$ [19–22]. The first-principles calculations found that $\beta$-$Bi_4I_4$ has a bulk electronic structure very similar to that of $\alpha$-$Bi_4I_4$, with a 3D Fermi surface in the valence band and a two-dimensional (2D) Fermi surface in the conduction band [23].

In this work, we carried out detailed studies on the angular and temperature dependence of magnetotransport properties of $\beta$-$Bi_4I_4$ with the steady and extrahigh pulsed magnetic field. Through SdH oscillations, we obtained a small cyclotron mass of $0.1\,m_e$, and a 3D angle mapping for magnetoresistivity (MR) reveals a convex Fermi surface. With the entrance of the extreme quantum limit (EQL), there occurs a metal-insulator transition. In the region far away from the EQL, the MR increases exponentially with regard to $\boldsymbol{B}$, and a field-induced effective gap is observed. Our findings indicate that $\beta$-$Bi_4I_4$ is possibly an ideal platform for exploring quantum limit physics and relevant exotic phases.

## II. EXPERIMENTAL SETUP

Single crystals of $\beta$-$Bi_4I_4$ were grown using the methods described in Ref. [17]. Starting materials Bi and $HgI_2$ powder with mole ratio 1:2 were mixed and finely ground in a

*shaoyh@szu.edu.cn
†zhangly@sustech.edu.cn

 ©2021 American Physical Society

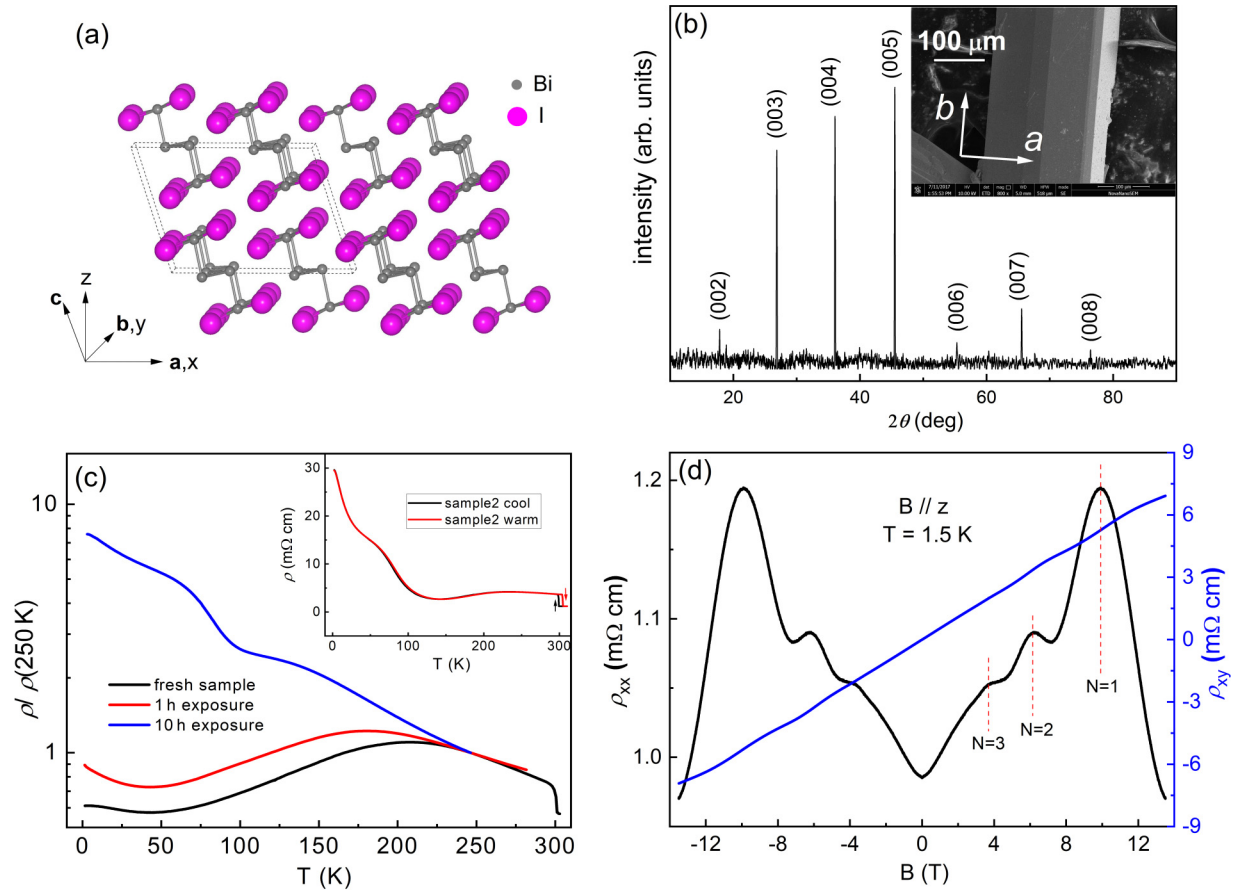


FIG. 1. (a) The $\beta$-$Bi_4I_4$ crystal in space group $C12/m1$ (No.12), with lattice parameters $a = 14.353$ Å, $b = 4.423$ Å, $c = 10.476$ Å, and $\beta = 107.8°$ between the $a$ and $c$ axes. Pink and gray spheres represent the bismuth and iodine ions, respectively, and the gray dashed box shows the unit cell. (b) The XRD pattern of $\beta$-$Bi_4I_4$ single crystals with $(00l)$ reflections. Inset: A scanning electron microscopy (SEM) image of a ribbon-shaped sample usually has quite irregular facets. (c) Temperature dependence of $\rho_{xx}$ curves normalized to $\rho$ (250 K) for sample 1 with different exposure times in the air. The fresh sample refers to the sample with the least exposure time, which was measured immediately after the contacts were made. Upper inset: Room temperature curves of sample 2 show the insulating behavior of the $\alpha$ phase. A hysteresis profile can be seen at 300 K. (d) $\rho_{xx}$ and $\rho_{xy}$ of sample 1 taken at 1.5 K; the magnetic field is parallel to the $z$ direction.

glove box, then loaded in a quartz tube 300 mm long and 16 mm in diameter. The quartz tube was flame sealed under high dynamic vacuum and placed into a two-zone furnace. A temperature gradient of 250 °C–210 °C was applied. After 20–30 days, the quartz tube was taken out and cooled in the air. Needlelike crystals with typical size 5 mm×0.3 mm×0.2 mm were obtained. The crystal structures and face index were examined by powder x-ray diffraction recorded by Rigaku SmartLab 9 KW with Cu $K\alpha$ radiation ($\lambda = 1.5406$ Å); average stoichiometry was determined by energy-dispersive x-ray spectroscopy. The transport properties under magnetic field were carried out in an Oxford TeslatronPT with temperature variable from 1.5 to 300 K and magnetic field up to 14 T. The 52 T pulsed magnetic field measurements were performed at Wuhan National High Magnetic Field Center. Before making the electrical connections, the crystal surface was cleaned by argon plasma followed by a deposition of 5/30 nm thick Cr/Au Hall bar pattern through a mask. Both the surface cleaning and Cr/Au deposition are crucial to the measurements, and it ensures the Ohmic contacts with a typical contact resistance of ∼1 Ω. By contrast, directly using silver paste resulted in large contact resistance of 0.2–2 kΩ, which increases further with time. This is possible because the surfaces of $\beta$-$Bi_4I_4$ are highly susceptible to the influence of moisture and organic solvent.

## III. RESULTS AND DISCUSSION

$\beta$-$Bi_4I_4$ has a quasi-one-dimensional (1D) structure, see Fig. 1(a), with Bi-I molecular chains stacked along both the $a$ and $c$ axes through weak noncovalent interactions. The chain's direction is along axis $b$, as indicated in the inset of Fig. 1(b). The average atomic ratio determined from energy-dispersive x-ray spectroscopy is Bi:I = 0.51:0.49, and no traces of mercury were detected on the cleaved surfaces. The structure of $\beta$-$Bi_4I_4$ is very similar to that of $\alpha$-$Bi_4I_4$. One crucial feature which distinguishes the $\alpha$ phase is the presence of (005) and (007) reflection peaks located at $2\theta \approx 22.3°$ and $2\theta \approx 31.5°$ [18,23]. Figure 1(b) shows that none of the two peaks is observed, confirming that our crystals are $\beta$-$Bi_4I_4$. Another feature that distinguishes these two phases is the temperature-dependent resistivity, with the $\alpha$ phase being much more resistive [18]. Figure 1(c) presents a typical curve of resistivity $\rho$ as a function of temperature $T$ for our $\beta$-$Bi_4I_4$ crystals.

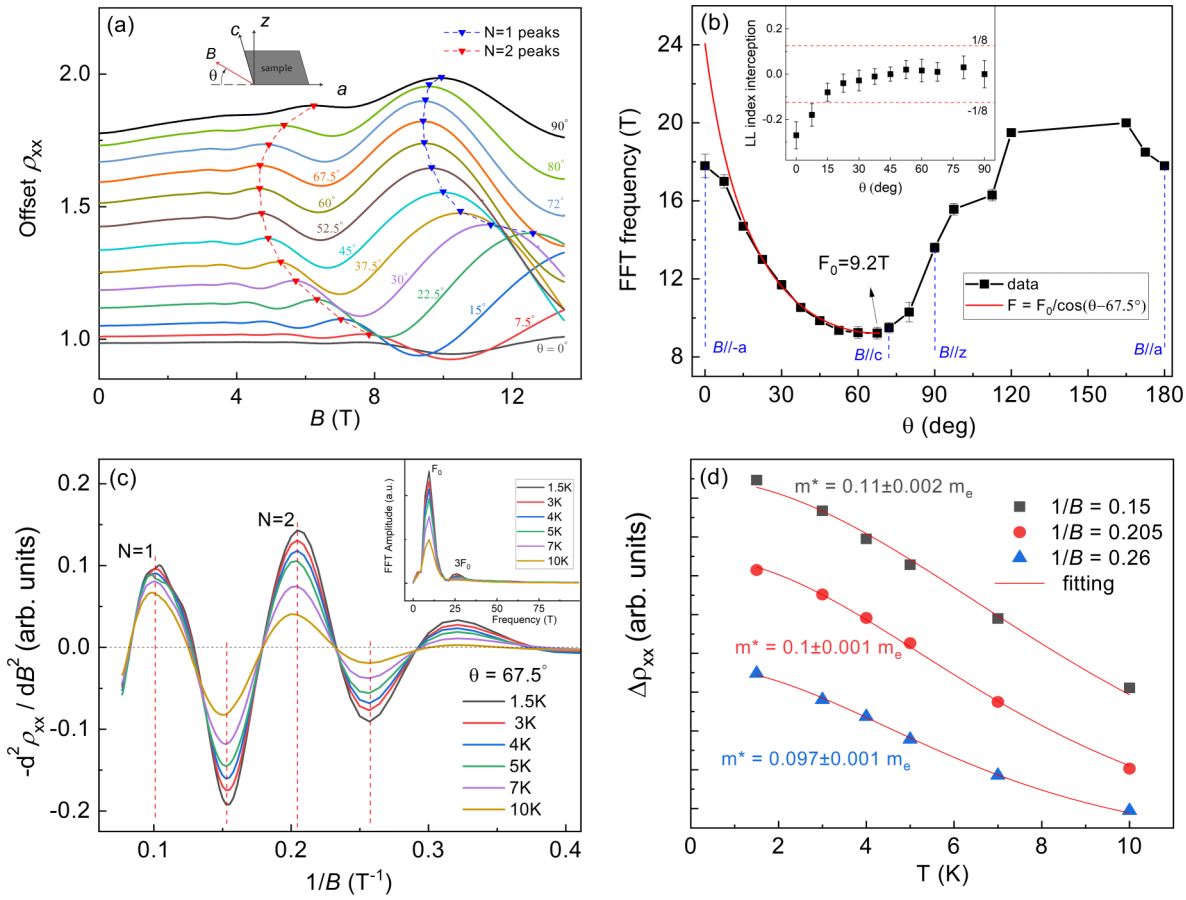


FIG. 2. (a) The angle dependence of the SdH oscillations from $\theta = 0°$ to $\theta = 90°$; the blue and red triangles mark the $N = 1$ and $N = 2$ Landau level peaks, respectively. (b) The obtained oscillation frequency as a function of $\theta$ from 0° to 180°. The red line draws the angle dependence of the frequency for a 2D Fermi surface; $F_0$ corresponds to the minimal cross-section area at $\theta = 67.5°$. The inset shows the interception extracted from the Landau level (LL) fan diagram. (c) $-d^2\rho_{xx}/d\boldsymbol{B}^2$ as a function of $1/\boldsymbol{B}$, at different temperatures ranging between 1.5 and 10 K. The inset shows the FFT transform of the data in the main panel. (d) The normalized oscillation amplitudes as a function of temperature, taken in different fields. The red line shows the fitting of the effective cyclotron mass following Lifshitz-Kosevich theory.

As $T$ decreases from room temperature, the resistivity of the freshly prepared samples (black line) usually forms a wide peak centered at around 200–220 K, followed by a metallic behavior down to 50 K, then increases again until the lowest temperature. As a comparison, we also present a $\rho(T)$ curve of another sample in the inset, a clear hysteretic loop at 300 K, and the much more resistive behavior below 200 K indicates the formation of $\alpha$-$Bi_4I_4$ after the phase transition at 300 K. We also found that resistivity is readily influenced by the environment. After warming up to 300 K and being exposed to the air for a period, the $\rho(T)$ changes with the peak shifts to lower temperature and the resistivity at low $T$ increases. The total 10 h of exposure (blue line) resulted in a semiconductor behavior quite similar to the $\alpha$-phase $Bi_4I_4$. We speculate that the reaction of iodine with moisture may change the surface conductivity.

We further characterize the sample with magnetotransport measurements. As shown in Fig. 1(d), when the magnetic field is applied along the $z$ direction, the longitudinal $\rho_{xx}$ shows clear SdH oscillations. At least three peaks can be distinguished, corresponding to the Landau level index $N = 3, 2$, and 1. Another prominent feature is that the $\rho_{xx}$ decrease sharply above $\boldsymbol{B} = 10.4$ T, to a negative MR region. A simple fast Fourier transform (FFT) analysis yields a single frequency, indicating that only one pocket is on the Fermi surface. The single-band nature is further confirmed by the Hall resistivity $\rho_{xy}$, which shows a linear behavior from −13.5 to 13.5 T. The bulk carrier density $n$ and the mobility $\mu$ at 1.5 K are obtained from the linear fitting of $\rho_{xy} = \boldsymbol{B}/ne$ and via $\sigma_0 = ne\mu$, which yield $n = 1.2\times10^{18}/\mathrm{cm}^3$ (hole type) and $\mu = 5400\,\mathrm{cm}^2\,\mathrm{V}^{-1}\,\mathrm{s}^{-1}$.

To understand the nature of the SdH oscillations, we performed magnetic field angle dependent measurements to tracked how the SdH oscillations shift with $\theta$ (the tilted angle between the magnetic field and the $-a$ axis). Figure 2(a) presents the $\rho_{xx}$ at different angles $\theta$; here all the curves have been shifted for clarity. As $\theta$ increases from 0 (where $B//-a$), the fields of $N = 1$ and $N = 2$ peaks decrease until $\theta = 67.5°$, then began to increase. The minimal angle 67.5° is very close to 72° between the (001) and (100) planes of $\beta$-$Bi_4I_4$. After an FFT analysis, the corresponding frequency as a function of $\theta$ is shown in Fig. 2(b). According to the Onsager relation $F = S_F\hbar/2\pi e$, the oscillation frequency is proportional to the extremal cross-section area of the Fermi surface $S_F$. For a two-dimensional (2D) Fermi surface, the oscillation frequency depends only on the field component

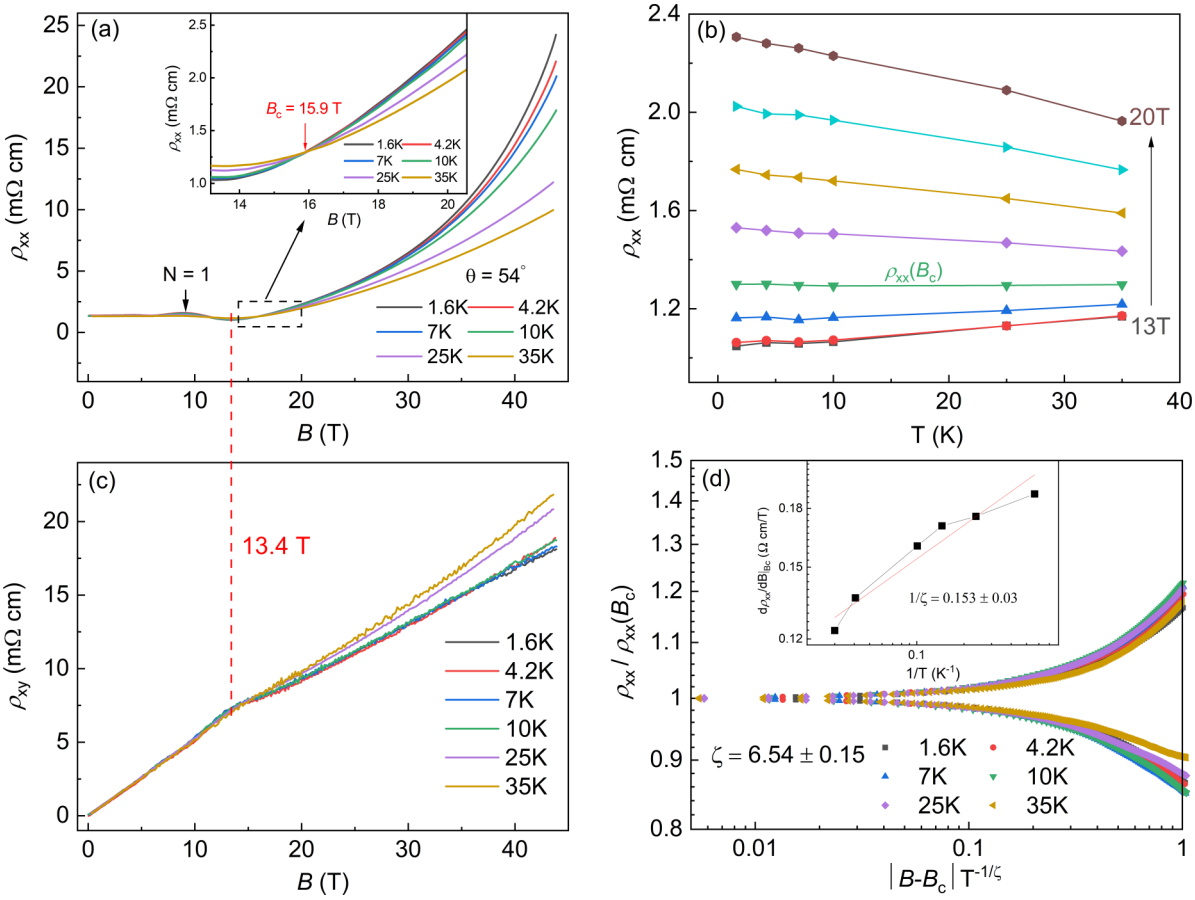


FIG. 3. (a) The field dependence of $\rho_{xx}$ up to 43 T under different temperatures. The red dashed line marks the ending of the quantum oscillation, above which the system enters the EQL. The inset shows the metal to insulator transition happens at a critical field of 15.9 T. (b) Plot of the $\rho_{xx}$ as a function of temperature at fixed magnetic field $\boldsymbol{B}$. (c) The field dependence of $\rho_{xy}$ up to 43 T. (d) Scaling plot of the normalized $\rho_{xx}$; all the isotherms fall onto a nearly single curve as a function of $|\boldsymbol{B}-\boldsymbol{B}_c|T^{-1/\zeta}$ with $\zeta \approx 6.5$; the inset shows the linear fitting of the $\log(\mathrm{d}\rho_{xx}/d\boldsymbol{B})$ at $B_c$ vs $\log(1/T)$, which yields $1/\zeta$.

$\boldsymbol{B} = \boldsymbol{B}_0\cos\theta$. As $\theta$ increase, the frequency will increase the following relation of $F(\theta) = F_0/\cos\theta$. Choosing the minimal frequency as $F_0$ when $\theta = 67.5°$ (which is 9.2 T), we have plotted the $F_0/\cos(\theta - 67.5°)$ in Fig. 2(b), as the red line shows. The measured data fit with the cosine relation only when $15° \leqslant \theta \leqslant 67.5°$, indicating that the oscillations originate from a 3D Fermi surface rather than a 2D, but with a convex shape. This is consistent with the first-principles calculation [23]. Fixing the angle at 67.5°, if we assume a circular Fermi surface cross section, the $k_F$ can be calculated from $S_F = \pi k_F^2$, which is $k_F = 1.7\times10^{-2}$ Å$^{-1}$. The inset in Figure 2(b) shows the interceptions obtained from the Landau level fan diagram, from which the Berry's phase can be determined. In a 3D system, an interception in the range of $\pm 1/8$ implies a nontrivial Berry's phase of $\pi$, and it is trivial otherwise. As the magnetic field tilted from $\boldsymbol{B}$//–a, the Berry's phase becomes nontrivial when $\theta \geqslant 15°$, in accordance with the ARPES results in Ref. [18], where the surface Dirac cone is found at the side surface [(100) surface] of the crystal.

After subtracting the background of $R_{xx}$ or $\rho_{xx}$ by taking a second derivative, the SdH amplitudes taken at different temperatures as a function of reciprocal $\boldsymbol{B}$ are presented in Fig. 2(c), along with the FFT spectrum. The cyclotron mass of carrier can be obtained by fitting the temperature dependence of the SdH amplitudes following Lifshitz-Kosevich (LK) theory:

$$A(T) = A_0 \frac{2\pi^2 k_B T/\hbar\omega_c}{\sinh(2\pi^2 k_B T/\hbar\omega_c)},$$

where $k_B$ is the Boltzmann's constant, and $\omega_c$ is the cyclotron frequency $\omega_c = e\boldsymbol{B}/m^*$. The effective cyclotron mass $m^*$ is determined to be $0.1m_0$ (where $m_0$ is the free electron mass) in Fig. 2(d).

Such a small effective mass implies large cyclotron energy $\hbar\omega_c$ in magnetic fields. When the field $\boldsymbol{B}$ is high enough that the criterion $\hbar\omega_c \gg E_F \gg k_B T$ is satisfied, the system enters the EQL where all the electrons occupy only the lowest Landau level. Experimentally, the EQL can be identified by the last peak of quantum oscillations on resistivity or thermoelectric curves [24,25]. In Fig. 1(d), $\rho_{xx}$ decreases sharply after the $N = 1$ peak at 10 T, suggesting that the system approaches the EQL. To investigate the quantum phases of $\beta$-$Bi_4I_4$ beyond the EQL, we further carried out the pulsed high magnetic field transport measurements up to 43 T, where the direction of magnetic field is pointed around the $c$ axis, as shown in Figs. 3(a) and 3(c). The quantum oscillations end up at 13.4 T with the $\rho_{xx}$ reaching the minima. Above 13.4 T, the $\rho_{xx}$ begins to increase monotonically without saturate; meanwhile

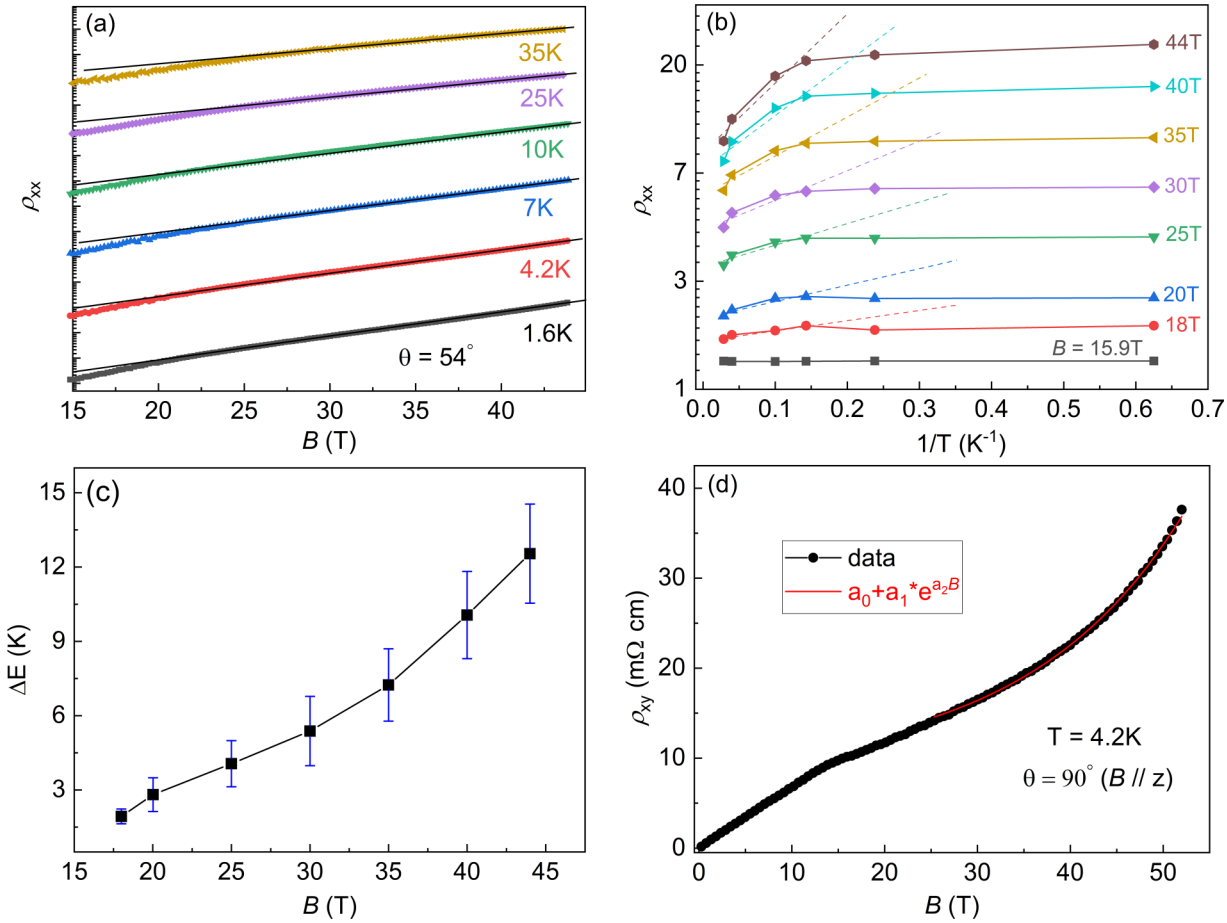


FIG. 4. (a) $\ln(\rho_{xx})$ as a function of field $\boldsymbol{B}$ up to 43 T; the curves have been shifted for clarity. The linear behavior above 20 T demonstrates the exponential increase of $\rho_{xx}$. (b) The Arrhenius plot of the temperature dependence of $\rho_{xx}$ under fixed magnetic field ranging from 15.9 to 43 T. (c) The energy gap is relative to a function of $\boldsymbol{B}$, and it increases almost linearly with the field. (d) The Hall resistivity up to 52 T at 4.2 K, where the field is parallel to the $z$ direction. Under high field, $\rho_{xx}$ also increase exponentially with $\boldsymbol{B}$; the red line draws a simple $e^{\boldsymbol{B}}$ fitting.

the Hall resistivity $\rho_{xy}$ changes its behavior from temperature independent to temperature dependent. We believe that both the sign change in $\rho_{xx}$ from negative to positive and the slope change in $\rho_{xy}$ indicate the system enters the EQL at 13.4 T, where the Fermi energy crosses only the lowest Landau level band $N = 0$ and lies right below the bottom of the band $N = 1$ [26]. As the magnetic field increases further, there exists a critical field of $\boldsymbol{B}_c = 15.9$ T where all the $\rho_{xx}$ curves taken at different temperatures share a common crossing point [Fig. 3(a), inset]. We also plot $\rho_{xx}$ as a function of temperature $T$ with fixed $\boldsymbol{B}$ ranging from 13 to 20 T, as shown in Fig. 3(b). Below the critical field $B_c$, the $\rho_{xx}$ decreases monotonically as $T$ decreases, while it increases when the field is above $\boldsymbol{B}_c$. This profile signals a metal-insulator transition at the critical field: The system is metallic below $\boldsymbol{B}_c$ and insulating above $\boldsymbol{B}_c$. Typically, for a magnetic field induced metal-insulator transition, the scaling relation of the resistivity to temperature and magnetic field can be described by [27,28]

$$\rho(\boldsymbol{B}, T) = \rho(B_c) f[|\boldsymbol{B} - \boldsymbol{B}_c| T^{-1/\zeta}],$$

where $f(x)$ is a scaling function with $f(0) = 1$, and $\zeta$ is the critical exponent which can be determined by evaluating the inverse slope of the log-log plot of $\frac{d\rho_{xx}}{d\boldsymbol{B}}|_{\boldsymbol{B}_c}$ vs $1/T$ [29]. With $B_c$ and $\zeta$ in hand, the scaling function can be directly tested without applying another fitting parameter. In Fig. 3(d), we performed such a scaling analysis, and indeed all the isotherms fall onto a nearly single curve as a function of $|\boldsymbol{B} - \boldsymbol{B}_c| T^{-1/\zeta}$. In the inset of Fig. 3(d), we obtained $1/\zeta = 0.153 \pm 0.03$ from the linear fitting of the data; this yields the critical exponent of $\zeta \approx 6.5$. According to a recent theory which describes the field-induced metal-insulator transition in 3D systems [30], a large critical exponent $\zeta \approx 6$ implies that strong electron-electron interactions may be involved at high fields.

In Fig. 4(a), however, with a much higher magnetic field $\boldsymbol{B}$ (>25 T), the $\rho_{xx}$ grows exponentially with increasing $\boldsymbol{B}$. We have ploted the logarithm resistivity $\ln(\rho_{xx})$ as a function of $\boldsymbol{B}$ under various temperatures (the curves have been shifted for clarity). It can be clearly seen that $\ln(\rho_{xx})$ increases linearly with $\boldsymbol{B}$ from 20–25 T to 43 T, depending on the sample temperature. This exponential increasing $\rho_{xx}$ is quite different from those $\boldsymbol{B}^2$, $\boldsymbol{B}$, or $\sqrt{\boldsymbol{B}}$ relations as usually seen in topological semimetals under high fields [31]. This new insulator region can be attributed to the magnetic freeze-out effect that led to a reduced carrier concentration. Typically, the magnetic freeze-out arises from the electron localization

in the extrinsic hopping conductivity region [32,33]. At low temperatures, the electrons are localized at impurity or dopant ions, and the conduction mechanism in these materials is variable range hopping between the impurity or dopant. The high magnetic field will further compress the wave functions of the localized states and reduce the overlap of the electron orbitals between neighbor ions, resulting in an exponential MR. Another mechanism for the magnetic freeze-out effect is an increasing effective energy gap with the field in an intrinsic narrow band-gap semiconductor with small carrier masses [34]. Under such conditions, at high fields where $\hbar\omega_c \gg k_B T$ holds, the carrier concentration decreases exponentially with magnetic field, $\frac{n(\boldsymbol{B})}{n(0)} \propto \exp(-\hbar\omega_c/4k_B T)$, which results in the exponentially increase of both $\rho_{xx}$ and $\rho_{xy}$ with field $\boldsymbol{B}$. Although both mechanisms exhibit an exponentially increasing magnetoresistivity, they are distinguishable in transport measurements. The distinctive evidence is that the argument of the exponential for the former is quadratic [35,32], while it is linear for the latter one [34]. In Fig. 4(b) we plot the $\ln(\rho_{xx})$ as a function of inverse temperature $1/T$ under fixed field $\boldsymbol{B}$, then fit the high temperature data to extract the effective band gap following Arrhenius plotting, $\rho_{xx} \propto \exp(\frac{\Delta}{2k_B T})$. The obtained band gap with error bars are shown in Fig. 4(c); it increases almost linearly with magnetic field from 0 K at 15.9 T to 12 K at 43 T. As a result, the concentration of the thermal carriers decreases which leads to the exponential behavior as shown in Fig. 4(a). This is further confirmed by the Hall resistivity [Fig. 4(d)], where the magnetic field up to 52 T is parallel to the $z$ axis. A clear nonlinear profile can be seen, and the high field data (>25 T) are proportional to $e^{\boldsymbol{B}}$. Our data support the magnetic freeze-out effect of the carrier concentration mechanism well beyond the EQL. However, as the impurities and defects are inherently present in crystals, both an intrinsic and extrinsic mechanism could be involved simultaneously in a particular sample. Further investigations are needed for better understanding in the near region of EQL.

## IV. CONCLUSION

In summary, we have investigated the magnetotransport properties of a small band-gap topological insulator $\beta$-$Bi_4I_4$ in a magnetic field up to 43 T. There exists a critical field $\boldsymbol{B}_c = 15.9$ T where metal to insulator transition happens. Below $\boldsymbol{B}_c$ the MR shows clear SdH oscillations, which reveals a 3D convex Fermi surface and a small effective hole mass of $0.1m_e$. In the near region of EQL, there is a metal-insulator transition around $\boldsymbol{B}_c$. Furthermore, the result of scaling analysis suggests that it results in a strong electron-electron transition. Far away from the EQL, both the longitudinal and Hall resistivity increase exponentially with field $\boldsymbol{B}$. The temperature dependence of the MR reveals an energy gap that increases linearly with field $\boldsymbol{B}$, which signifies the magnetic freeze-out of carrier concentration, where the system has a narrow bulk energy gap. The extract mechanisms of the transitions observed here still require further investigation.

## ACKNOWLEDGMENTS

We thank Haizhou Lu, Kun Yang, and Haiwen Liu for their enlightening discussions. The work was supported by Guangdong Innovative and Entrepreneurial Research Team Program (Grant No. 2016ZT06D348), NFSC (Grant No. 11874193), China postdoctoral Science Foundation (Grant No. 2020M672760), and Shenzhen Fundamental subject research Program (Grant No. JCYJ20170817110751776). X.D. acknowledges support from NSF under Grant No. DMR-1808491.

[1] L. Fu, C. L. Kane, and E. J. Mele, Topological Insulators in Three Dimensions, Phys. Rev. Lett. **98**, 106803 (2007).

[2] J. C. Y. Teo, L. Fu, and C. L. Kane, Surface states and topological invariants in three-dimensional topological insulators: Application to $Bi_{1-x}Sb_x$, Phys. Rev. B **78**, 045426 (2008).

[3] D. Hsieh, Y. Xia, D. Qian, L. Wray, J. H. Dil, F. Meier, J. Osterwalder, L. Patthey, J. G. Checkelsky, N. P. Ong, A. V. Fedorov, H. Lin, A. Bansil, D. Grauer, Y. S. Hor, R. J. Cava, and M. Z. Hasan, A tunable topological insulator in the spin helical Dirac transport regime, Nature **460**, 1101 (2009).

[4] Y. L. Chen, J. G. Analytis, J. H. Chu, Z. K. Liu, S. K. Mo, X. L. Qi, H. J. Zhang, P. H. Lu, X. Dai, Z. Fang, S. C. Zhang, I. R. Fisher, Z. Hussain, and Z. X. Shen, Experimental realization of a three-dimensional topological insulator, $Bi_2Te_3$, Science **325**, 178 (2009).

[5] H. Zhang, C.-X. Liu, X.-L. Qi, X. Dai, Z. Fang, and S.-C. Zhang, Topological insulators in $Bi_2Se_3$, $Bi_2Te_3$ and $Sb_2Te_3$ with single Dirac cone on the surface, Nat. Phys. **5**, 438(2009).

[6] P. Cheng, C. Song, T. Zhang, Y. Zhang, Y. Wang, J. F. Jia, J. Wang, Y. Wang, B. F. Zhu, X. Chen, X. Ma, K. He, L. Wang, X. Dai, Z. Fang, X. Xie, X. L. Qi, C. X. Liu, S. C. Zhang, and Q. K. Xue, Landau Quantization of Topological Surface States in $Bi_2Se_3$, Phys. Rev. Lett. **105**, 076801 (2010).

[7] J. Chen, H. J. Qin, F. Yang, J. Liu, T. Guan, F. M. Qu, G. H. Zhang, J. R. Shi, X. C. Xie, C. L. Yang, K. H. Wu, Y. Q. Li, and L. Lu, Gate-Voltage Control of Chemical Potential and Weak Antilocalization in $Bi_2Se_3$, Phys. Rev. Lett. **105**, 176602 (2010).

[8] J. G. Checkelsky, Y. S. Hor, R. J. Cava, and N. P. Ong, Bulk Band Gap and Surface State Conduction Observed in Voltage-Tuned Crystals of the Topological Insulator $Bi_2Se_3$, Phys. Rev. Lett. **106**, 196801 (2011).

[9] H. T. He, G. Wang, T. Zhang, I. K. Sou, G. K. L. Wong, J. N. Wang, H. Z. Lu, S. Q. Shen, and F. C. Zhang, Impurity Effect on Weak Antilocalization in the Topological Insulator $Bi_2Te_3$, Phys. Rev. Lett. **106**, 166805 (2011).

[10] D. X. Qu, Y. S. Hor, J. Xiong, R. J. Cava, and N. P. Ong, Quantum oscillations and Hall anomaly of surface states in the topological insulator $Bi_2Te_3$, Science **329**, 821 (2010).

[11] J. G. Analytis, R. D. McDonald, S. C. Riggs, J. H. Chu, G. S. Boebinger, and I. R. Fisher, Two-dimensional surface state in the quantum limit of a topological insulator, Nat. Phys. **6**, 960 (2010).

[12] Z. Ren, A. A. Taskin, S. Sasaki, K. Segawa, and Y. Ando, Large bulk resistivity and surface quantum oscillations in the topological insulator $Bi_2Te_2Se$, Phys. Rev. B **82**, 241306 (2010).

[13] H. Peng, K. Lai, D. Kong, S. Meister, Y. Chen, X. L. Qi, S. C. Zhang, Z. X. Shen, and Y. Cui, Aharonov-Bohm interference in topological insulator nanoribbons, Nat. Mater. **9**, 225 (2010).

[14] F. Xiu, L. He, Y. Wang, L. Cheng, L. Te Chang, M. Lang, G. Huang, X. Kou, Y. Zhou, X. Jiang, Z. Chen, J. Zou, A. Shailos, and K. L. Wang, Manipulating surface states in topological insulator nanoribbons, Nat. Nanotechnol. **6**, 216 (2011).

[15] Z. Li, Y. Qin, F. Song, Q. H. Wang, X. Wang, B. Wang, H. Ding, C. Van Haesondonck, J. Wan, Y. Zhang, and G. Wang, Experimental evidence on the Altshuler-Aronov-Spivak interference of the topological surface states in the exfoliated $Bi_2Te_3$ nanoflakes, Appl. Phys. Lett. **100**, 083107 (2012).

[16] C. C. Liu, J. J. Zhou, Y. Yao, and F. Zhang, Weak Topological Insulators and Composite Weyl Semimetals: $\beta$-$Bi_4X_4$ ($X$ = Br, I), Phys. Rev. Lett. **116**, 066801 (2016).

[17] G. Autès, A. Isaeva, L. Moreschini, J. C. Johannsen, A. Pisoni, R. Mori, W. Zhang, T. G. Filatova, A. N. Kuznetsov, L. Forró, W. Van Den Broek, Y. Kim, K. S. Kim, A. Lanzara, J. D. Denlinger, E. Rotenberg, A. Bostwick, M. Grioni, and O. V. Yazyev, A novel quasi-one-dimensional topological insulator in bismuth iodide $\beta$-$Bi_4I_4$, Nat. Mater. **15**, 154 (2016).

[18] R. Noguchi, T. Takahashi, K. Kuroda, M. Ochi, T. Shirasawa, M. Sakano, C. Bareille, M. Nakayama, M. D. Watson, K. Yaji, A. Harasawa, H. Iwasawa, P. Dudin, T. K. Kim, M. Hoesch, V. Kandyba, A. Giampietri, A. Barinov, S. Shin, R. Arita *et al.*, A weak topological insulator state in quasi-one-dimensional bismuth iodide, Nature **566**, 518 (2019).

[19] A. Pisoni, R. Gaál, A. Zeugner, V. Falkowski, A. Isaeva, H. Huppertz, G. Autès, O. V. Yazyev, and L. Forró, Pressure effect and superconductivity in the $\beta$-$Bi_4I_4$ topological insulator, Phys. Rev. B **95**, 235149 (2017).

[20] X. Wang, J. Wu, J. Wang, T. Chen, H. Gao, P. Lu, Q. Chen, C. Ding, J. Wen, and J. Sun, Pressure-induced structural and electronic transitions in bismuth iodide, Phys. Rev. B **98**, 174112 (2018).

[21] Y. Qi, W. Shi, P. Werner, P. G. Naumov, W. Schnelle, L. Wang, K. G. Rana, S. Parkin, S. A. Medvedev, B. Yan, and C. Felser, Pressure-induced superconductivity and topological quantum phase transitions in a quasi-one-dimensional topological insulator: $Bi_4I_4$, npj Quantum Mater. **3**, 4 (2018).

[22] S. Deng, X. Song, X. Shao, Q. Li, Y. Xie, C. Chen, and Y. Ma, First-principles study of high-pressure phase stability and superconductivity of $Bi_4I_4$, Phys. Rev. B **100**, 224108 (2019).

[23] D. Y. Chen, D. S. Ma, Y. Li, Z. Z. Du, X. Xiong, Y. He, J. X. Duan, J. Han, D. Chen, W. Xiao, and Y. Yao, Quantum transport properties in single crystals of $\alpha$-$Bi_4I_4$, Phys. Rev. Mater. **2**, 114408(2018).

[24] T. Liang, Q. Gibson, J. Xiong, M. Hirschberger, S. P. Koduvayur, R. J. Cava, and N. P. Ong, Evidence for massive bulk Dirac fermions in $Pb_{1-x}Sn_xSe$ from Nernst and thermopower experiments, Nat. Commun. **4**, 2696 (2013).

[25] F. Tang, Y. Ren, P. Wang, R. Zhong, J. Schneeloch, S. A. Yang, K. Yang, P. A. Lee, G. Gu, Z. Qiao, and L. Zhang, Three-dimensional quantum Hall effect and metal–insulator transition in $ZrTe_5$, Nature **569**, 537 (2019).

[26] H. Li, H. He, H. Z. Lu, H. Zhang, H. Liu, R. Ma, Z. Fan, S. Q. Shen, and J. Wang, Negative magnetoresistance in Dirac semimetal $Cd_3As_2$, Nat. Commun. **7**, 10301 (2016).

[27] S. L. Sondhi, S. M. Girvin, J. P. Carini, and D. Shahar, Continuous quantum phase transitions, Rev. Mod. Phys. **69**, 315 (1997).

[28] D. M. Finlayson, Metal-insulator transition in InP, Philos. Mag. Lett. **61**, 293 (1990).

[29] A. F. Hebard and M. A. Paalanen, Magnetic-Field-Tuned Superconductor-Insulator Transition in Two-Dimensional Films, Phys. Rev. Lett. **65**, 927 (1990).

[30] P.-L. Zhao, H.-Z. Lu, and X. C. Xie, Theory for magnetic-field-driven 3D metal-insulator transitions in the quantum limit, arXiv:2012.12541.

[31] H. Z. Lu and S. Q. Shen, Quantum transport in topological semimetals under magnetic fields, Front. Phys. **12**, 127201 (2017).

[32] M. L. Knotek, High-field magnetoresistance of hopping transport in the disordered impurity system of transmutation-doped Ge, Phys. Rev. B **16**, 2629 (1977).

[33] N. Mikoshiba, Strong-field magnetoresistance of impurity conduction in $n$-type germanium, Phys. Rev. **127**, 1962 (1962).

[34] N. Spector, Quantum-limit magnetoresistance in intrinsic semiconductors, Phys. Rev. B **25**, 3822 (1981).

[35] V. F. Mitin, V. V. Kholevchuk, and E. A. Soloviev, High positive magnetoresistance in Ge films at low temperatures, Appl. Phys. Lett. **110**, 012102 (2017).